

Direct Numerical Simulations of Droplet Impact onto Heated Surfaces using the Program Free Surface 3D (FS3D)

Manish Kumar, Rishav Saha, Johanna Potyka, Kathrin Schulte and Bernhard Weigand

Abstract Droplet impact onto heated surfaces is a widespread process in industrial applications, particularly in the context of spray cooling techniques. Therefore, it is essential to study the complex phenomenon of droplet spreading, heat removal from a hot surface, and flow distribution during the impact. This study focuses on Direct Numerical Simulation (DNS) of the initial stage of a water droplet impact onto a highly conducting heated surface, below the saturation temperature of the liquid. The maximum spreading diameters at different impact velocities in the presence of a heated surface, are analysed. Free Surface 3D (FS3D), an in-house code developed at the Institute of Aerospace Thermodynamics, University of Stuttgart, is used for this work. A grid independence study investigates the resolution required to resolve the flow field around the droplet. As evaporation effects during the initial stage of the droplet impact process are negligible, they are ignored. However, for longer simulation times, evaporation plays a significant role in the process. Preparing for such simulations, an evaporating droplet in cross flow is simulated to study the performance gain in the newly implemented hybrid OpenMP and MPI parallelisation and red-black optimization in the evaporation routines of FS3D. Both the scaling limit and efficiency were improved by using the hybrid (MPI with OpenMP) parallelisation, while the red-black scheme optimization raised the efficiency only. An improved performance of 23% of the new version is achieved for a test case investigated with the tool MAQAO. Additionally, strong and weak scaling performance tests are conducted. The new version is found to scale up to 256 nodes compared to 128 nodes for the original version. The maximum time-cycles per hour (CPH) achieved with the new version is 35% higher compared to the previous version.

Manish Kumar and Rishav Saha
Institute of Aerospace Thermodynamics (ITLR), University of
Stuttgart, Pfaffenwaldring 31, 70569 Stuttgart, Germany, e-mail:
manish.kumar@itlr.uni-stuttgart.de and rishav.saha@itlr.uni-stuttgart.de

1 Introduction

The interaction between droplets and heated surfaces is a subject of significant interest across various scientific and technological fields. When a liquid droplet at room temperature contacts a hot surface, the temperature difference creates a heat flow from the surface toward the droplet. The heat flow gives a cooling effect on the surface, a beneficial effect commonly utilized in industrial applications such as spray cooling [11]. The extent of heat transfer mostly depends on the temperature difference and the contact area. However, determining the contact area and the time scale associated with it is a well-known droplet dynamics problem. This process is influenced by numerous factors, including droplet parameters (such as diameter, impact velocity, and physical properties like saturation temperature, density, viscosity, and surface tension), surrounding gas parameters (such as pressure, temperature, and relative humidity), and surface characteristics (including wettability, diffusivity, surface roughness, and temperature) [14, 12]. Among these factors, the droplet impact velocity and the surface temperature are the most crucial parameters governing the impact dynamics and the heat transfer process [3]. Hence, further investigations are required to understand the fundamentals of the droplet impact onto heated surfaces.

Under atmospheric conditions, a drop impacting perpendicularly to a flat wall will show a splashing, spreading, or bouncing behavior [6], depending on the impact velocity. Splashing occurs when a droplet impacts a surface at a high velocity, causing the droplet to break apart. In case of lower impact velocities, however, the droplet spreads out smoothly over the surface without breaking apart into smaller ligaments. This results in a larger contact area between the droplet and the surface, enhancing the efficiency of the heat transfer [4]. Therefore, investigating the spreading phase is crucial. Based on the surface temperatures, four distinct regimes can be identified: film evaporation, nucleate boiling, transition boiling and film boiling [16, 13]. When the surface temperature is below the saturation temperature of the liquid (film evaporation), the heat transfer is dominated by heat conduction. Surface temperatures above this range lead to vapour bubbles and boiling. Therefore, to investigate the wetting behaviour fundamentally, it is worth considering the film evaporation regime, where boiling effects can be ignored.

According to the droplet evaporation time, the film evaporation regime is commonly divided into three stages, initial, fundamental and final [10, 24]. In the initial stage, the spreading, recoiling and oscillation of the droplet is observed, until it forms a stable spherical liquid cap. Subsequently, the three-phase contact line remains pinned, which involves cap evaporation with diminishing contact angle and droplet height. Finally, the residual liquid rapidly shrinks and complete evaporation is observed. Studies show that the initial stage of droplet impact is faster and dominated by inertia [24]. During this stage, the droplet reaches its maximum contact area, significantly influencing the overall heat transfer rate. Therefore, the initial stage, where maximum wetting occurs, is considered critical for studying the process. In addition, during this period, internal convection [23] of the droplet, airflow around the liquid [2] also plays a significant role in the process.

In the present work, a single droplet of pure water at atmospheric conditions impacts perpendicularly onto a smooth isothermal surface at 363 K. The study

focuses on the initial stage of the impact process to capture the maximum spreading at high Weber and Reynolds numbers. These simulations are challenging due to the wide range of time and length scales involved. This requires high spatial and temporal resolutions, which can only be achieved with an efficient parallelization of the code and the use of high-performance computing clusters. The DNS is conducted using the in-house multiphase flow solver FS3D running on a supercomputer of the High Performance Computing Center Stuttgart (HLRS), the HPE Apollo (Hawk). Later in the report, Section 4 presents the computational performance gains achieved through newly implemented optimization and parallelization techniques in FS3D evaporation routines. Evaporation routines are required for future work in cases where evaporation cannot be ignored for droplet wetting on heated surfaces.

2 Methods

2.1 Governing equations

The conservation equations solved for mass and momentum are given for this one-field approach by,

$$\rho_t + \nabla \cdot (\rho \mathbf{u}) = 0, \quad (1)$$

$$[\rho \mathbf{u}]_t + \nabla \cdot [\rho \mathbf{u} \mathbf{u}] = \nabla \cdot [\mathbf{S} - \mathbf{I}p] + \rho \mathbf{g} + \mathbf{f}_\gamma, \quad (2)$$

with \mathbf{u} denoting the velocity vector, ρ the density, p the static pressure, \mathbf{S} the viscous stress tensor and \mathbf{g} the gravitational acceleration. \mathbf{f}_γ represents the surface forces in the vicinity of the interface [5]. An incompressible Newtonian fluid is assumed. The energy equation solved in its temperature form reads as

$$\frac{\partial(\rho c_p T)}{\partial t} + \nabla \cdot (\rho c_p T \mathbf{u}) = \nabla \cdot (k \nabla T) + q, \quad (3)$$

where k is the heat conductivity, T is the temperature, c_p is the specific heat at constant pressure and q is a source term. The Volume of Fluid (VOF) method by Hirt and Nichols [9] is applied to distinguish between the different phases by introducing the volume fraction, f ,

$$f(\mathbf{x}, t) = \begin{cases} 0 & \text{in the disperse phase,} \\ (0, 1) & \text{for interfacial cells,} \\ 1 & \text{in the continuous phase} \end{cases} \quad (4)$$

that represents the amount of the liquid in each cell. A transport equation for f needs to be solved to obtain the phase distribution over time,

$$\partial_t f + \nabla \cdot (f \mathbf{u}) = 0. \quad (5)$$

To increase the accuracy of the corresponding f -fluxes, the Piecewise Linear Interface Calculation (PLIC) method by Rider and Kothe [21], which calculates the orientation and position of the interface in each cell is used.

2.2 Simulation tool: FS3D

The DNS is conducted using the in-house multiphase flow solver FS3D [7] running on a supercomputer of the High-Performance Computing Center Stuttgart (HLRS), HPE Apollo Hawk platform. The incompressible Navier-Stokes equations and the energy equation [7, 22, 20] in temperature formulation are solved using the Finite-Volume method, where the interface is captured using the VOF method with the PLIC reconstruction [9] in a Cartesian grid. Separate temperature fields are solved for both phases [25]. The continuum surface force (CSF) model [5] is used to account for surface tension, while the interface reconstruction is performed using the piecewise linear interface calculation (PLIC) method [21]. FS3D has been developed at the Institute of Aerospace and Thermodynamics for more than 25 years and has been applied successfully to various multiphase flow problems like droplet impacts onto structured surfaces [18], evaporating droplets [26], thermocapillary flows [15] and drop-film interactions [8]. To simulate such processes, a high spatial and temporal resolution as well as large computational domains are necessary. Therefore, the code is parallelized with MPI and OpenMP, and it is continuously optimized to increase its parallel efficiency and scaling on high-performance clusters.

2.3 Computational Setup

A droplet of diameter D is initialized in a cubic domain of size $2D$ with an initial droplet velocity of V . Initially, the droplet is at a distance of $0.1D$ above the bottom hot surface. The symmetry of the droplet impact dynamics is leveraged to study the behavior of droplets impacting a heated surface. Hence, a quarter droplet is simulated instead of the whole droplet. Figure 1 shows a two-dimensional schematic diagram and a three-dimensional view of the computational domain, detailing the initialized configuration.

Table 1: Physical properties of air and water used, where ρ , μ and c_p represent density, dynamic viscosity and specific heat at constant pressure, respectively.

	ρ (kg/m ³)	μ (Pas)	c_p (kJ/(kgK))
Air	1.184	$1.825 \cdot 10^{-5}$	1.006
Water	997	$8.921 \cdot 10^{-4}$	4.18

A pure water droplet of spherical shape is considered to have an initial diameter of $D = 2$ mm. The numerical setup assumes that the fluid dynamics of water and surrounding air are incompressible and Newtonian. The properties of both fluids (air and water) are listed in Table 1, and the surface tension coefficient (σ) is considered to be 72 mN/m. At the moment, constant fluid properties are used because of the small temperature differences involved. The surrounding ambient of the droplet is at 1 atmospheric pressure, and the initial temperature is 298 K. The gravitational force (g) acts in the downward direction. Continuous boundary conditions were applied to the far faces of the domain except for symmetric planes and the bottom

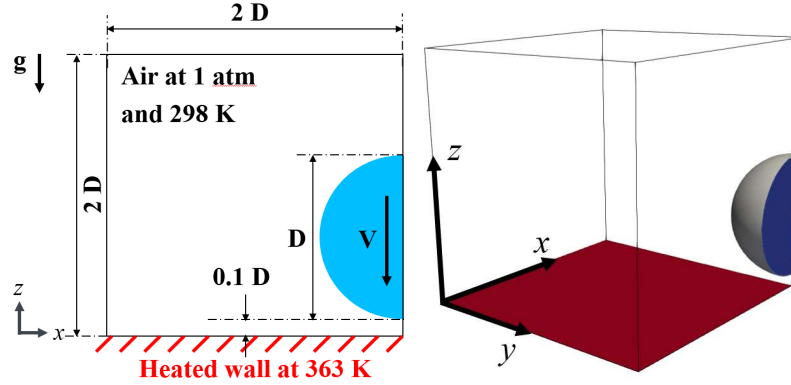


Fig. 1: (Left) Schematic 2D diagram of the computational domain with domain configuration at the initial point. (Right) 3D visualization of the computational domain showing a quarter of the droplet, with the hot surface highlighted in red.

surface. The bottom surface is assumed to be of high conductive substrate, and an isothermal boundary condition is enforced at the temperature of 363 K, below the boiling temperature of the water. Evaporation is ignored as the time scale of evaporation is large compared to the wetting time scale. Droplet impact dynamics is studied at different impact velocities, and these values are listed in Table 2, as well as the corresponding values of Weber number (We) and Reynolds number (Re). We and Re are defined as $We = \rho_w V^2 D / \sigma$ and $Re = \rho_w V D / \mu_w$, respectively, where the subscript w represents water.

Table 2: Investigated droplet impact velocities and corresponding values of Weber and Reynolds numbers.

Cases	I	II	III	IV	V
V in m/s	1	1.5	2	2.5	3
We	27	62	110	173	250
Re	2230	3350	4470	5590	6705

3 Results and Discussion

3.1 Grid independence study

A grid independence study is presented in the following to determine the influence of the grid resolution on the simulations. Four grid sizes were investigated in the study. Details of the different grid sizes are listed in Table 3. Grid sizes were increased systematically by a factor of two, from 128 to 1024 in each direction of the cubic domain, which resulted in a systematic increase in the number of cells from two million to one billion. Hence, the number of cells per initial drop diameter was varied from 64 cells to 512 cells.

Table 3: Details of different grids employed for the grid independence study.

	GRID 128	GRID 256	GRID 512	GRID 1024
Grid size	128×128×128	256×256×256	512×512×512	1024×1024×1024
Number of cells	2 million	17 million	134 million	1 billion
Resolution in cells/ D	64	128	256	512

The case with the highest impact velocity is chosen to evaluate the grid independence. Figure 2 shows a snapshot of one such simulation and indicates the locations of line probes L1 and L2. The location of probe L1 is placed outside the droplet (at 2.8 mm from the right boundary), and probe L2 is placed inside the droplet (at 2 mm from the right boundary) so that both regions' velocity and temperature fields can be compared. These fields are compared at an intermediate time, $t = 0.84$ ms, when the droplet is still spreading.

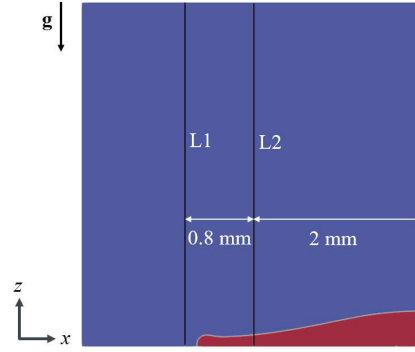


Fig. 2: Snapshot of droplet simulation at time $t = 0.84$ ms indicating the location of probes L1 and L2 at which simulation parameters are compared for the grid independence study.

Figure 3a and 3b show the velocity magnitude and temperature variation along the z -axis and probe L1, in case of different grid sizes, respectively. For all grid sizes, the velocity magnitude increases, and starts to decrease after reaching a maximum value. However, temperature decreases monotonically and in a non-linear fashion. Also, it can be observed from Figure 3a that as the grid size increases from 128 to 1024, velocity profiles start to converge in the case of GRID 512 and GRID 1024. However, grid independence can be achieved from GRID 256 in the case of temperature, as shown in Figure 3b. Temperature data for GRID 128 is not plotted in figure 3b, as the temperature solution diverges for this coarse grid size.

Similarly, Figures 4a and 4b show the velocity magnitude and the temperature profile at probe line L2. The temperature in Figure 4b is plotted till 0.01 cm of z -axis coordinate within the droplet region where large differences can be seen and compared among different grid sizes. Satisfactory grid independence is achieved

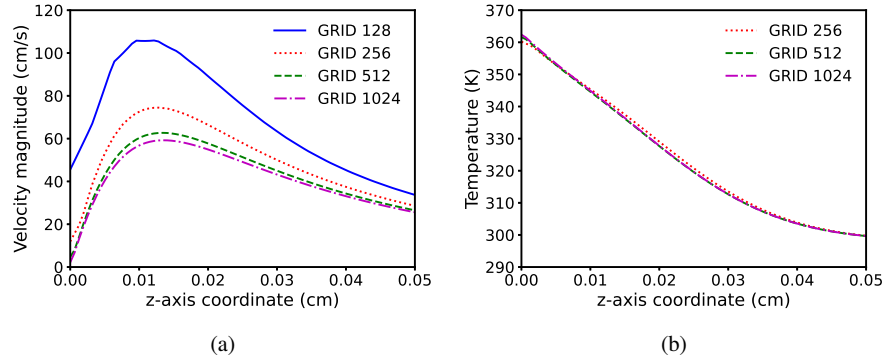


Fig. 3: (a) Velocity magnitude and (b) temperature profile along z-axis calculated using different grid sizes at probe line L1.

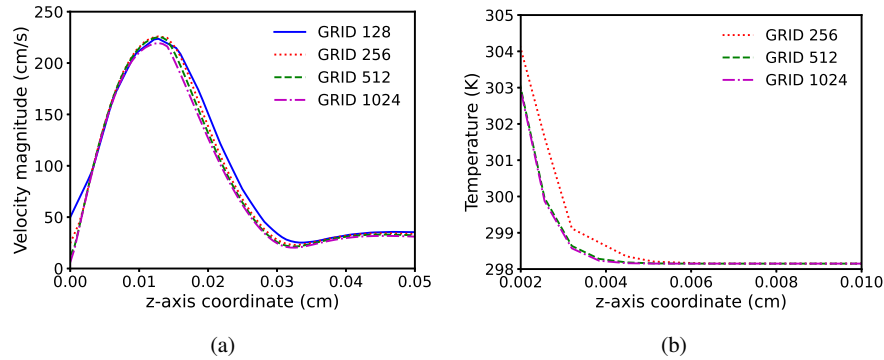


Fig. 4: (a) Velocity magnitude and (b) temperature profile along z-axis calculated using different grid sizes at probe L2.

from grid size GRID 256 in the case of velocity, as shown in Figure 4a. On comparing Figure 4a and 3a, it can also be observed that the velocity magnitude is higher inside the droplet compared to the ambient air. In the case of the temperature profile, grid independence was achieved from GRID 512. Hence, the present study uses GRID 512 for all simulations to study the droplet impact onto a heated surface.

3.2 Droplet spreading

Figure 5 shows the wetting dynamics of droplets (in red color) impacting onto a heated surface in a quiet ambient air (in blue color). Time-sequenced images show how the droplets spread at different impact speeds, denoted by the corresponding Weber number. It can be observed from Figure 5 that the droplet spreads rapidly until 0.72 ms, and after that, the spreading slows down until the droplet reaches its maximum spreading diameter. Capillary waves can be observed at the liquid-gas interface of the droplet. As the droplet spreads, droplet liquid rushes towards

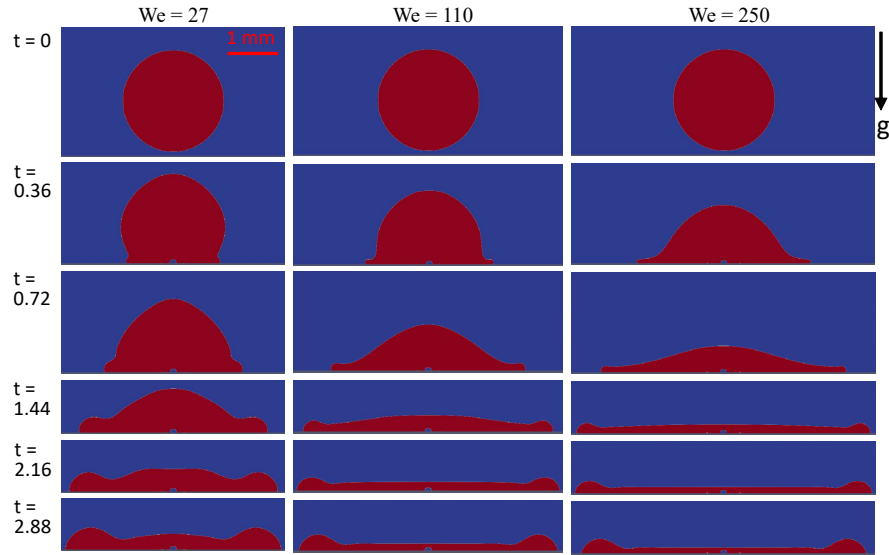


Fig. 5: Time-sequenced snapshots of droplet impact simulations for three cases of Weber numbers (i.e. 27, 110, and 250). The time (t) is provided in the first column of frames in milliseconds (ms).

the periphery of the droplet, creating a rim. The rim formation happens due to the high kinetic energy of the droplet impact, which tries to dominate over dissipating effects of droplet liquid, i.e., viscosity and surface energy. As the Weber number (We) increases, the droplet spreads faster and achieves a larger wetting diameter compared to an impact at a lower Weber number.

The quantification of the dimensionless wetting diameter (d/D) variation with respect to dimensionless time ($\tau = t.V/D$) for different Weber numbers (We) is shown in Figure 6a. The droplet wetting diameter increases non-linearly for all Weber numbers. As explained earlier, it can also be seen in Figure 6a that the maximum wetting diameter increases with increasing Weber numbers. In the case of a higher Weber number, the droplets attain the maximum wetting diameter earlier than in the lower Weber number cases. In the cases of $We = 173$ and 250 , the droplet attains the maximum wetting diameter around 1.5 ms and starts to recede around 1.8 to 2 ms. However, in the case of $We = 27$ and 62 , the droplet attains its maximum wetting diameter at 2.8 ms.

Figure 6b shows the effect of Reynolds number (Re) on the non-dimensional spreading parameter called the spreading factor (β). The spreading factor (β) is defined as the ratio of the maximum wetting diameter to the initial diameter of the spherical droplet before the impact. The variation of spreading factor (β) with respect to $Re^{1/5}$ is shown in Figure 6b. A linear dependence of β can be observed, which indicates the viscous regime of droplet spreading [14].

From the heat transfer perspective, it is clear from figures 3b and 4b, that the maximum water temperature reached is significantly lower than the maximum air

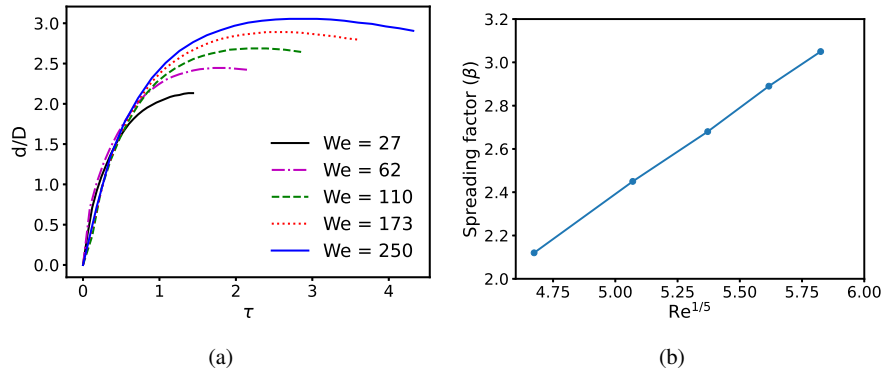


Fig. 6: (a) Dimensionless wetting diameter (d/D) variation of the droplet with respect to dimensionless time ($\tau = t.V/D$), for different cases of Weber numbers (We). (b) Variation of spreading factor (β) with respect to the Reynolds number (Re).

temperature. This is because the specific heat of water is greater than that of air. Additionally, only a thin portion of the liquid film, around 20% of its height, is heated. This indicates that the heating process is slower than the droplet spreading. In the future, more focus will be kept on the heat transfer part and the consideration of a possible influence of the temperature-dependent fluid properties.

All simulations with GRID 512 utilizes 8 MPI processes in each x , y and z -direction, which corresponds to a total of 512 MPI processes. Four nodes were used with 128 MPI processes for a wall-time of 11.4, 13.6, 15.6, 16.5, and 17.2 hours for Cases I, II, III, IV and V, respectively.

4 Computational Performance

Continuous enhancements of FS3D's performance are necessary to keep pace with advancements in super-computing hardware and the demands of increasingly larger simulation domains and resolutions. Several performance optimization techniques within FS3D have previously focused on the most time-consuming routines of the hydrodynamics solver, including the multigrid (MG) solver, viscosity solver, and momentum advection solvers [27, 28, 17]. However, for the study of heat and mass transfer [19, 20], optimizing the phase transfer (evaporation) routines is crucial to enhance the overall performance. This is especially important when the evaporation timescale becomes comparable to other physical phenomena, such as droplet wetting. In the latest version of FS3D, evaporation routines are optimized with a Red-black scheme and OpenMP implementation.

4.1 Red-black scheme and OpenMP implementation in evaporation routines

In a previous work on optimising the hydrodynamics solver of FS3D, Potyka et al. [17] found that a significant speed-up for loops employing red-black schemes

can be achieved. If the order of operations is organized such that the data required for the second, black iteration does not have to be loaded from main memory, a speed-up by up to a factor of two is possible. This can be achieved by slice-wise progress of the red and black iterations through the three-dimensional arrays, where the black iteration follows the red iteration with an offset of one slice. An analysis in the phase change solver identified that a red-black scheme as one of the most time-consuming routines. Hence, the above-described cache-blocking approach was adapted for the red-black Gauss-Seidel smoother solving for the conducted heat. Which resulted in a reduction of the computational time by 29% for the test case described in Sec. 4.2. The obtained gain is below the theoretical value of $\approx 50\%$ reduction in computational time achievable with perfect cache reuse. The equation solved in this routine requires eleven three-dimensional arrays, and seven of them are accessed with a seven-point stencil. Therefore, the benefit is lower than the optimum. Nevertheless, this re-organization of only one loop translates to a reduction of the overall compute time of FS3D by 5.4% for the test case described in Sec. 4.2.

In some cases, the MPI-process communication may govern computational time consumption and the scaling limit. Reducing the number of MPI processes per node, while keeping a constant problem size, increases the domain size per MPI process while reducing the MPI communication and memory usage for the halo data employed for the boundary conditions. Using fewer MPI processes per node leads to a reduction of used resources, if only MPI is employed for the parallelization. Implementing a hybrid parallelisation approach that combines MPI with OpenMP allows a reduction of MPI processes while still utilizing all available cores. FS3D was previously parallelized with OpenMP to run on vector computers and will run on GPU machines in the near future. We have since enhanced and revised the OpenMP parallelisation in FS3D's most time-consuming routines of the evaporation solver by implementing OpenMP at the loop level. As a result, multiple costly MPI communications are no longer necessary, and the shared memory among OpenMP threads reduces the amount of MPI halo data blocking memory. This at first suggests the usage of only one MPI process per ccNUMA node. However, other hardware limitations must be considered. For example, on HPE Apollo (Hawk), four CPU cores (CCX) share a common Level 3 (L3) cache, but beyond that caches are not shared. As tested and concluded in a previous report [28], four OpenMP threads per MPI process are considered optimal on the chosen hardware. Eight OpenMP threads do not share the Level 3 cache, resulting in costly memory transfers due to the absence of a "first-touch" principle implementation. Consequently, the following performance study utilizes four OpenMP threads per MPI process.

4.2 Test-case description

Evaporation of a liquid droplet in a gaseous cross-flow is considered for the performance test of evaporation (or liquid-gas phase change) routines. The computational domain of the same is shown in Figure 7. A spherical droplet with an initial temperature of 280.85 K, lower than the ambient air, is placed in a cubic domain containing the continuous phase (air). The initial ambient temperature of the air is 297.65 K.

The droplet is also subjected to a cross flow of the air having a velocity of 0.571 m/s and a temperature of 297.65 K, which is the same as the initial temperature of the ambient air. Hence, on the left face of the computational domain, the inflow boundary condition and on the right face, a pressure outlet boundary condition is applied. The other faces of the domain are subjected to continuous far-field boundary conditions.

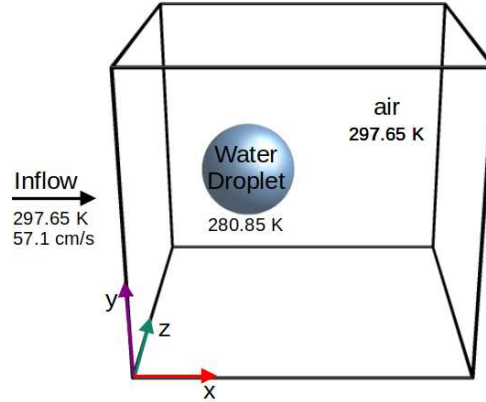


Fig. 7: Computational domain of the test case used for performance evaluation of the evaporation routines in FS3D.

4.3 Computational time consumption evaluation

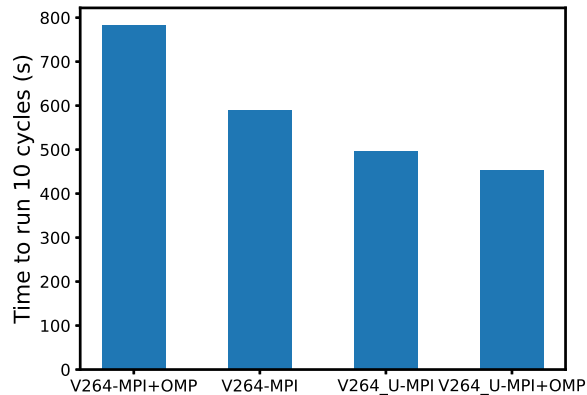


Fig. 8: Performance of different version of FS3D tested for running 10 time cycles.

The performance enhancements were implemented in FS3D version V264. The updated version is named V264_U in this report for convenience. Both versions were compiled with the GNU compiler (version 10.2.0) using MPI with OpenMP (MPI+OMP) and without OpenMP to compare the performance in each case. The performance analysis tool MAQAO [1] was used to evaluate the performance of

the different versions of FS3D on HPE Apollo (Hawk). The size of the grid for the further analyzed test case was $256 \times 256 \times 256$. 128 MPI processes in the case of only MPI and 32 MPI processes with 4 OpenMP threads in the case of MPI+OMP were employed for the analysis with MAQAO on a single node of HPE Apollo (Hawk). This ensured the testing of both versions was performed on the same computational resources. Figure 8 shows the total time taken to compute 10-time cycles with the different versions of FS3D. It can be observed from the bar chart in Figure 8 that version V264_U takes less computational time compared to V264 in both cases with and without OpenMP. Also, the MPI+OMP parallelized version of V264_U results in the lowest observed time to solution. This shows, that the introduced optimizations discussed above are beneficial to the overall compute time of FS3D in this specific case. The following investigates the scaling behavior of the different versions presented above.

4.4 Strong scaling performance

The effect of increasing the number of cores on the performance is measured by performing a strong scaling, i.e., keeping the grid size fixed while increasing the parallelization. A fixed spatial resolution of $1024 \times 1024 \times 1024$ grid cells was chosen for the following. Figure 9a shows the measured strong scaling performance on a log-plot. Figure 9a shows cycles per hour (CPH) calculated by FS3D for the same test case as described in section 4.2 using two modes of parallelization, i.e., MPI and MPI+OMP. The CPH represents the time steps (cycles) simulated per hour. The test cases' simulations were made to run for 30 minutes to measure and extrapolate CPH. Note that each node of HPE Apollo (Hawk) has 128 CPU cores. In the MPI cases without OpenMP, the simulations were performed with one MPI process per core using full nodes. For cases using MPI with OpenMP, a parallelization with four OpenMP threads per MPI-process and 32 MPI processes per node was employed, hence again the full nodes were employed. Each MPI-process is pinned with a stride of four for the four OpenMP threads. This arrangement allows for a comparison of the usage of the same computational resources, solving the same problem size with an identical resolution, but using different parallelization techniques and FS3D versions with and without the newly introduced optimizations. The number of nodes for parallelization was systematically increased to measure the CPH until the CPH started to decline for increasing allocated resources for each combination of the FS3D version and the parallelization technique. The largest number of nodes employed for the strong scaling investigation was 512 nodes, i.e., 65536 CPU cores.

Figure 9a shows that the CPH increases monotonically for all combinations until 128 cores. V264 with MPI+OMP shows the lowest CPH compared to other combinations. V264_U with only MPI shows the best performance with 16 and 32 nodes, while V264_U with MPI+OMP shows the best performance for all other numbers of nodes. All combinations except V264_U with MPI+OMP start to show a performance decrease with 256 nodes. For V264_U with MPI+OMP, the CPH increases until 256 nodes and then decreases with 512 nodes. This shows that the hybrid implementation not only improves the performance for previously used numbers of

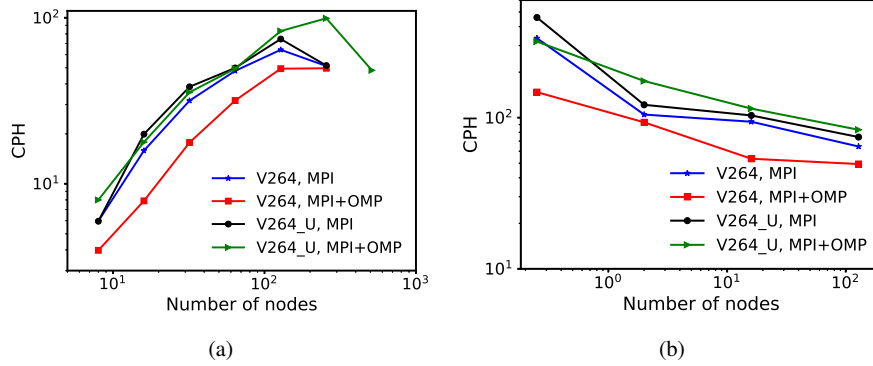


Fig. 9: (a) Strong scaling performance, (b) Weak scaling performance: Estimated cycles per hour (CPH) in case of utilizing MPI and MPI with OpenMP for both versions V264 and V264_U.

nodes but also improves the strong scaling limit of usable resources by a factor of two. The maximum CPH attained with V264_U is 35% higher compared to V264.

4.5 Weak scaling performance

In the weak scaling, the number of cells per processing core is kept constant. Hence, with an increase in the number of processing cores (or nodes), the number of cells was increased with the number of CPU cores employed. The same test case for strong scaling was used to perform a weak scaling test in the present work using 65536 cells per CPU core. Each MPI+OMP parallelization had four times the number of grid cells in MPI parallelization so that each core had the same number of cells to process. Thereby, the same computational resources were used to process the same problem size for all combinations.

Figure 9b shows the weak scaling. It can be observed that the updated version V264_U with MPI+OMP computes more CPH than the original version V264 for both types of parallelization techniques when running with 4 to 128 nodes. In the case of 4 nodes, the CPH of V264_U with MPI+OMP was 67% higher than V264 with MPI. However, in the case of a quarter node (32 CPU cores), V264_U with MPI performs the best, indicating better computation efficiency by a pure MPI parallelization, if not the full node is employed and communication is not the bottleneck anymore.

5 Conclusions

The wetting dynamics of droplets impacting onto a heated surface are presented using DNS simulations. The simulations were performed using the in-house DNS code FS3D. FS3D can be used for high spatial and temporal resolution as it has been parallelized using MPI and OpenMP. A grid-independence study was conducted to

ensure that the results were not influenced by the grid resolution. A grid size of $512 \times 512 \times 512$ was found to be sufficient enough to adequately resolve the impact dynamics of droplets considered in the present study. The impact dynamics of droplets were investigated for the range of Weber numbers from 27 to 250 and Reynolds numbers from 2230 to 6705. For this range of We and Re , the droplet wets the surface smoothly in a spreading regime without showing any splashing. As the droplet spreads, it forms a rim at the edge of the droplet as it attains the maximum diameter. The maximum wetted diameter of the droplet increases linearly with $Re^{1/5}$. It is also observed that during spreading, only a very thin portion of the liquid film is heated, indicating that the heat conduction timescale is slower than the inertial timescale of the process for the parameter variation studied here.

In some cases, droplet impact on the heated surface may involve strong evaporation dynamics with a smaller time scale of evaporation. Therefore, it is necessary to increase the overall performance of the code for longer simulation times. The "MAQAO" tool was used on HPE Apollo (HAWK) to measure the computational time required by a new optimized version (V264_U) and the original version (V264) of FS3D to run 10 time-cycles with two parallelization techniques, i.e., MPI and MPI+OMP. The V264_U version with MPI+OMP shows the best performance with a decrease of 23% in computational time. Two optimizations were introduced: The hybrid parallelization using MPI with four OpenMP threads per MPI process, reduces the overall MPI communication time and memory usage for halo data. This accounts for a reduction of 17.6%. Employing a re-organization of a loop using a red-black scheme leads to a 5.4% reduction of FS3D's overall runtime. Strong and weak scaling of both versions were also evaluated. The V264_U version showed improved scaling by a factor of 2 compared to V264. The V264_U version can scale efficiently to 256 nodes with no drop in the performance.

Acknowledgments

The authors kindly acknowledge the *High Performance Computing Center Stuttgart* (HLRS) for support and supply of computational resources on the HPE Apollo (Hawk) platform under the Grant No. FS3D/11142. Additionally, the authors gratefully acknowledge the financial support of the Deutsche Forschungsgemeinschaft (DFG, German Research Foundation) under Germany's Excellence Strategy EXC2075-390740016 through the project 409029509, "Investigation of Droplet Motion and Grouping" and through the project 270852890, GRK2160: "Droplet Interaction Technologies (DROFIT)".

References

1. Maqao (modular assembly quality analyzer and optimizer). URL <https://www.maqao.org/>. Accessed: 24-05-2024
2. Berberović, E., Roisman, I.V., Jakirlić, S., Tropea, C.: Inertia dominated flow and heat transfer in liquid drop spreading on a hot substrate. *Int. J. Heat Fluid Flow.* **32**(4), 785–795 (2011)

3. Bernardin, J.D., Stebbins, C.J., Mudawar, I.: Mapping of impact and heat transfer regimes of water drops impinging on a polished surface. *Int. J. Heat Mass Transfer.* **40**(2), 247–267 (1997)
4. Bonn, D., Eggers, J., Indekeu, J., Meunier, J., Rolley, E.: Wetting and spreading. *Rev. Mod. Phys.* **81**(2), 739 (2009)
5. Brackbill, J.U., Kothe, D.B., Zemach, C.: A continuum method for modeling surface tension. *J. Comput. Phys.* **100**(2), 335–354 (1992)
6. Breitenbach, J., Roisman, I.V., Tropea, C.: From drop impact physics to spray cooling models: a critical review. *Exp. Fluids.* **59**, 1–21 (2018)
7. Eisenschmidt, K., Ertl, M., Gomaa, H., Kieffer-Roth, C., Meister, C., Rauschenberger, P., Reitzle, M., Schlottke, K., Weigand, B.: Direct numerical simulations for multiphase flows: An overview of the multiphase code FS3D. *Appl. Math. Comput.* **272**, 508–517 (2016)
8. Fest-Santini, S., Steigerwald, J., Santini, M., Cossali, G., Weigand, B.: Multiple drops impact onto a liquid film: Direct numerical simulation and experimental validation. *Computers & Fluids.* **214**, 104761 (2021)
9. Hirt, C.W., Nichols, B.D.: Volume of fluid (vof) method for the dynamics of free boundaries. *J. Comput. Phys.* **39**(1), 201–225 (1981)
10. Hu, H., Larson, R.G.: Evaporation of a sessile droplet on a substrate. *J. Phys. Chem. B.* **106**(6), 1334–1344 (2002)
11. Jia, W., Qiu, H.H.: Experimental investigation of droplet dynamics and heat transfer in spray cooling. *Exp. Therm. Fluid Sci.* **27**(7), 829–838 (2003)
12. Josserand, C., Thoroddsen, S.T.: Drop impact on a solid surface. *Annu. Rev. Fluid Mech.* **48**, 365–391 (2016)
13. Ko, Y., Chung, S.: An experiment on the breakup of impinging droplets on a hot surface. *Exp. Fluids* **21**(2), 118–123 (1996)
14. Liang, G., Mudawar, I.: Review of drop impact on heated walls. *Int. J. Heat Mass Transfer.* **106**, 103–126 (2017)
15. Ma, C., Bothe, D.: Direct numerical simulation of thermocapillary flow based on the volume of fluid method. *Int. J. Multiphase Flow.* **37**(9), 1045–1058 (2011)
16. Naber, J.D., Farrell, P.V.: Hydrodynamics of droplet impingement on a heated surface. *SAE Transactions* pp. 1346–1361 (1993)
17. Potyka, J., Stober, J., Wurst, J., Ibach, M., Steigerwald, J., Weigand, B., Schulte, K.: Towards DNS of droplet-jet collisions of immiscible liquids with FS3D. In: *High Performance Computing in Science and Engineering '22*, pp. 197–212. Springer (2022)
18. Ren, W., Foltyn, P., Geppert, A., Weigand, B.: Air entrapment and bubble formation during droplet impact onto a single cubic pillar. *Sci. Rep.* **11**(1), 18018 (2021)
19. Reuttsch, J., Ertl, M., Baggio, M., Seck, A., Weigand, B.: Towards a Direct Numerical Simulation of Primary Jet Breakup with Evaporation, chap. 16, pp. 243–257. Springer (2019)
20. Reuttsch, J., Kieffer-Roth, C., Weigand, B.: A consistent method for direct numerical simulation of droplet evaporation. *Journal of Computational Physics* **413**, 109455 (2020)
21. Rider, W.J., Kothe, D.B.: Reconstructing volume tracking. *J. Comput. Phys.* **141**(2), 112–152 (1998)
22. Rieber, M.: Numerische Modellierung der Dynamik freier Grenzflächen in Zweiphasenströmungen. Dissertation, Universität Stuttgart (2004)
23. Ruiz, O.E., Black, W.Z.: Evaporation of water droplets placed on a heated horizontal surface. *J. Heat Transfer* **124**(5), 854–863 (2002)
24. Rymkiewicz, J., Zapalowicz, Z.: Analysis of the evaporation process for water droplet on flat heated surface. *Int. Commun. Heat Mass Transfer.* **20**(5), 687–697 (1993)
25. Schlottke, J.: Direkte Numerische Simulation von Mehrphasenströmungen mit Phasenübergang. Verlag Dr. Hut (2010)
26. Schlottke, J., Dulger, E., Weigand, B.: A vof-based 3d numerical investigation of evaporating, deformed droplets. *Prog. Comput. Fluid Dyn.* **9**(6-7), 426–435 (2009)
27. Steigerwald, J., Ibach, M., Reuttsch, J., Weigand, B.: Towards the Numerical Determination of the Splashing Threshold of Two-component Drop Film Interactions. Springer (2022)
28. Stober, J.L., Potyka, J., Ibach, M., Weigand, B., Schulte, K.: DNS of the early phase of oblique droplet impact on thin films with FS3D. In: *High Performance Computing in Science and Engineering '23*. Springer (2023)